

A Non-Local Low-Rank Framework for Ultrasound Speckle Reduction

Lei Zhu¹, Chi-Wing Fu^{1,3}, Michael S. Brown², and Pheng-Ann Heng^{1,3}

¹The Chinese University of Hong Kong, ²York University,

³Shenzhen Key Laboratory of Virtual Reality and Human Interaction Technology,
 Shenzhen Institutes of Advanced Technology, Chinese Academy of Sciences, China

{lzhu, cwfu, pheng}@cse.cuhk.edu.hk, mbrown@eecs.yorku.ca

Abstract

‘Speckle’ refers to the granular patterns that occur in ultrasound images due to wave interference. Speckle removal can greatly improve the visibility of the underlying structures in an ultrasound image and enhance subsequent post-processing. We present a novel framework for speckle removal based on low-rank non-local filtering. Our approach works by first computing a guidance image that assists in the selection of candidate patches for non-local filtering in the face of significant speckles. The candidate patches are further refined using a low-rank minimization estimated using a truncated weighted nuclear norm (TWNN) and structured sparsity. We show that the proposed filtering framework produces results that outperform state-of-the-art methods both qualitatively and quantitatively. This framework also provides better segmentation results when used for pre-processing ultrasound images.

1. Motivation and Related Work

Medical ultrasound is a widely used noninvasive imaging modality that can reveal internal anatomic structures. Ultrasound makes use of a transducer to emit ultra-high-frequency sound waves, which change direction when a reflective surface is encountered. Careful timing of the emitted sound signal and its observed echo is used to determine the anatomical structures. One drawback of ultrasound imaging is the ‘speckle’ that results from wave interference when the scattered waves constructively and destructively combine to produce the black and white spot pattern characteristic of ultrasound images [3, 14]. Fig. 1 shows a typical ultrasound image and the speckle pattern.

The presence of speckles lowers the overall image quality and makes the interpretation of ultrasound images challenging for nonspecialists [23, 31]. Like noise, speckle can also adversely affect the identification of normal and pathological tissues by trained specialists [8, 20]. Furthermore, it lowers the accuracy of computer-aided diagnosis [8] and

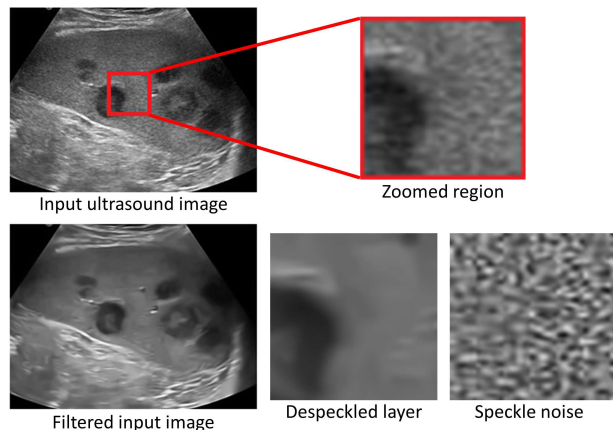


Figure 1: **Top** A typical clinical ultrasound image corrupted with speckles. **Bottom** The despeckled and speckle noise layers recovered by our proposed method.

adversely affects subsequent image processing tasks such as segmentation [2, 5]. Ultrasound speckle patterns usually contain information on the microstructure, but, to be fair, being able to remove speckles as a pre-processing step allows a much larger range of existing methods to be directly applied; see Section 3.3 for our segmentation example.

Over the last two decades there have been a number of methods proposed to reduce speckle noise. A number of wavelet-based methods have been proposed to decompose the ultrasound image into frequency subbands and then use various strategies to filter wavelet coefficients associated with speckle noise (see [7] for an overview of wavelet-based methods). However, these frequency domain approaches tend to oversmooth the image details by filtering excessive frequencies, or produce ringing artifacts due to removal of incorrect bands [33].

Another popular strategy for speckle removal are local image filtering methods. Among these methods, the most successful ones are those based on anisotropic diffusion (e.g., [20, 8, 32]) and the bilateral filter (e.g., [2]). While local filters are successful for speckle reduction, their performance suffers in the presence of strong noise, which

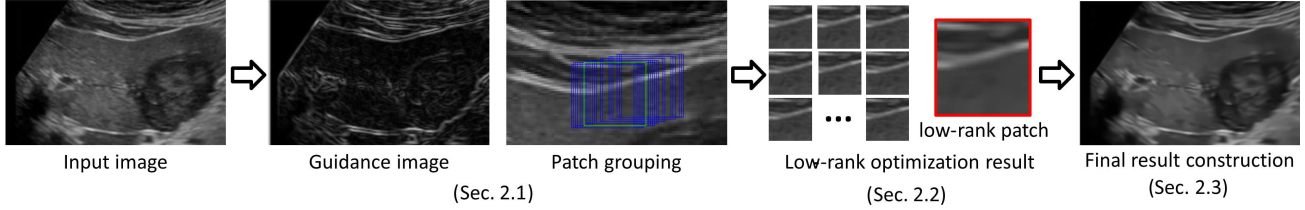


Figure 2: An overview of our non-local low-rank filtering framework. First, we compute a guidance image to help locate the candidate patches (Sec. 2.1). Then, we refine the patches to recover the low-rank structure (Sec. 2.2) and aggregate the low-rank patches to construct the final filtered result (Sec. 2.3).

corrupts the correlations between neighboring pixels [10]. In addition to local filtering, non-local filtering methods have also been proposed. Methods such as non-local means (NLM) [5, 33, 30] leverage the entire image by finding similar patches in a larger neighborhood of a target pixel. The collection of patches is then used to filter the target pixel. These non-local self-similarity (NSS) approaches are sensitive to the quality of the selected patches and can produce blurry results if poorly similar patches are selected.

Recently, a number of NLM filters have been developed for various image processing tasks by combining NSS and low-rank priors - e.g. image denoising [9], video denoising [12], multispectral image denoising [27], and image deblurring [6]. These methods, however, target natural images and often have problems in finding candidate patches due to the severity of the speckle noise patterns present in ultrasound images. The success of these non-local methods serves as the starting point of our filtering framework.

Contributions. We propose a novel non-local filtering framework for speckle noise reduction. Due to the noisy nature of ultrasound images, non-local filtering methods could perform poorly when selecting candidate patches. To overcome this problem, our approach first pre-filters the input image to produce a guidance image to improve the patch selection quality. We further formulate a low-rank optimization model to process the selected patches, where the noise is considered to be sparse with the clear patch being low-rank. We describe how to modify existing low-rank optimization methods to accommodate the noisy nature of speckle noise. To verify the effectiveness of the proposed method, we test it on a number of synthetic and clinical ultrasound images, and compare our results against several state-of-the-art methods. We also evaluate our method in terms of a segmentation accuracy. Our approach shows notable improvement on a range of image quality metrics.

2. Proposed Filtering Framework

Fig. 2 provides an overview of our proposed filtering framework. The framework begins by computing a guidance image to improve the search for candidate patches as described in Sec. 2.1. A ‘clear patch’ is estimated from the candidate patches by estimating a low-rank and sparse rep-

resentation of the patch collection as described in Sec. 2.2. Lastly, the final despeckled image is produced by aggregating the restored patches as described in Sec. 2.3.

2.1. Non-local Patch Selection

Given a reference patch in the input image, the non-local patch selection process aims to find a group of patches similar to the reference patch based on some distance metric. Due to the large intensity variations caused by the speckle noise, direct application of the Euclidean distance is not effective. In other medical imaging modalities, such as MRI, it has been demonstrated that a pre-filtered version of the input can serve as a guidance image to assist in non-local patch selection [17]. The key is to find an appropriate method to generate the guidance image for the image modality at hand. Since speckle noise has a granular texture-like pattern, we employ the windowed inherent variation (WIV) measure [29] to generate the guidance image, G , from the input image I as follows:

$$G(p) = \sqrt{|\sum_q g_{p,q} \cdot (\partial_x I)_q|^2 + |\sum_q g_{p,q} \cdot (\partial_y I)_q|^2}, \quad (1)$$

where p is a pixel in I , q is a pixel in the rectangular neighborhood centered at p , and $g_{p,q}$ is a weighting function based on spatial affinity, which is defined as $g_{p,q} \propto \exp(-\frac{\text{dist}_{p,q}}{2\sigma_w^2})$, where σ_w controls the spatial scale of the neighboring rectangle.

In general, a patch dominated by speckle noise has a small G value compared to patches with structure and features. The reason is that speckle noise is observed as a texture-like pattern with dark and bright intensities. Such a pattern leads to a large amount of positive and negative partial derivatives in all directions, while structured edges in a patch contribute to gradients in more similar directions. With the WIV-guidance image, we compute the distance between two non-local patches centered at pixels p and q as:

$$\text{dist}(p, q) = \|P_I(p) - P_I(q)\| \cdot \|P_G(p) - P_G(q)\|, \quad (2)$$

where $\|\cdot\|$ represents the L_2 norm, and $P_I(p)$, $P_I(q)$, $P_G(p)$ and $P_G(q)$ are the vectorized patches centered at pixels p and q in image I and guidance image G , respectively.

The purpose of the guidance image is to improve patch selection in noisy ultrasound images. As demonstrated in

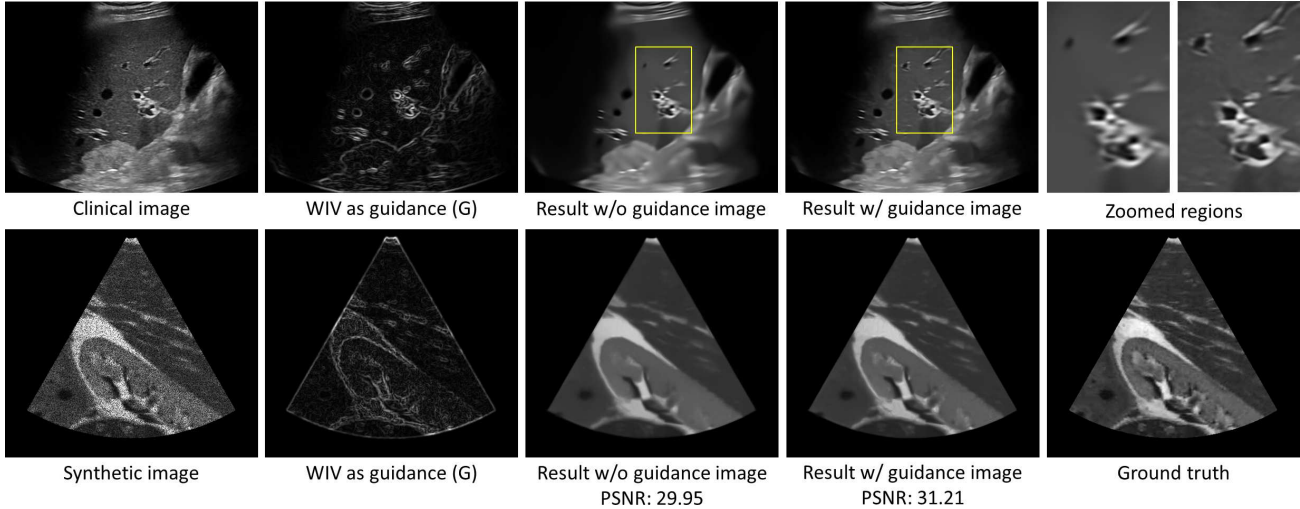


Figure 3: Comparing the final despeckled results with and without the use of guidance image on a clinical (top) and synthetic (bottom) ultrasound image as inputs; the synthetic image input is corrupted by a synthetic speckle noise model [5].

Fig. 3, the speckle noise is heavily suppressed in the WIV map, since features have larger filter response than speckle noise. While this filtered image is not suitable as a despeckled result, it serves as a good guidance image. In particular, we can see that the despeckled results are improved when using the WIV in Fig. 3. Only using the input image to measure patch similarity is inefficient to separate patches centered at features from speckle noise dominated patches, leading to feature blurring. With the patch distance defined in Eq. 2, we select the K most similar patches for each patch in the input image. In our implementation, the window for searching similar patches is $(2 \times S_w + 1) \times (2 \times S_w + 1)$ with $S_w = 20$ to reduce the computation time. In all the experiments, we set $K = 30$ and patch size as 7×7 .

2.2. Low-Rank Patch Recovery

After finding the K most similar patches $\{P_i\}_{i=1}^K$ (in image I) for a given reference patch P_{ref} , we construct a patch group (PG) matrix Ψ_I :

$$\Psi_I = [V(P_{ref}), V(P_1), V(P_2), \dots, V(P_K)], \quad (3)$$

where $V(\cdot)$ vectorizes a patch as a 49-element column vector. Similarly, we denote Ψ_D as the PG matrix for each pixel in the final despeckled image D . Our observation on the ultrasound images is that Ψ_D should be a low-rank matrix due to the strong correlation between patches after speckle removal. However, due to the speckle noise, the rank of Ψ_I (the raw input) tends to be high. Therefore, we formulate a low-rank recovery process to estimate Ψ_D from Ψ_I . That is, we decompose Ψ_I into a low-rank component (Ψ_D) and a sparse component (Ψ_η) by solving:

$$\min_{\Psi_D, \Psi_\eta} \text{rank}(\Psi_D) + \alpha \|\Psi_\eta\|_0 \text{ s.t. } \Psi_I = \Psi_D + \Psi_\eta, \quad (4)$$

where $\text{rank}(\Psi_D)$ denotes the rank of Ψ_D , which equals to the L_0 norm of the singular values of Ψ_D ; and α is a weight

to balance the two regularization terms. The second sparse term is introduced to the low-rank recovery process to improve the robustness of the method against outliers caused by noise artifacts and patch grouping error.

Truncated weighted nuclear norm. The foregoing L_0 optimization is known to be NP-hard [1]. Robust principle component analysis (RPCA) [26] is a common way to solve it in a tractable way by approximating the rank operation ($\text{rank}(\Psi_D)$) using the nuclear norm $\|\Psi_D\|_*$, which is defined as the sum of all the singular values of Ψ_D . Note that in our implementation, we use SVD to decompose Ψ_D to obtain the singular values of Ψ_D .

In practice, the rank operation may not be well approximated using the nuclear norm [34, 9], since it minimizes all singular values equally. As a result, important image features, which correspond to large singular values, will become blurred because their corresponding singular values will be minimized extensively according to the nuclear norm. Therefore, we should assign smaller weights to larger singular values, so that their magnitude can be maintained after the minimization; this is also suggested in [9]. Similarly, the smallest singular values, which correspond to noise, can be simply removed, as suggested in [34].

In this regard, we formulate a truncated and weighted nuclear norm (TWNN), $\|\cdot\|_{tw}$, to better approximate the rank operator by combining the strength of the truncated nuclear norm [34] and the weighted nuclear norm [9]:

$$\|\Psi_D\|_{tw} = \sum_{i=1}^M w_i \sigma_i(\Psi_D), \quad (5)$$

where M is the total number of the singular values; and w_i is the weight for the i -th singular value σ_i of Ψ_D . Since we use SVD, M equals to the minimum of $K + 1$ and d^2 , which are the dimensions of the PG matrix Ψ_I .

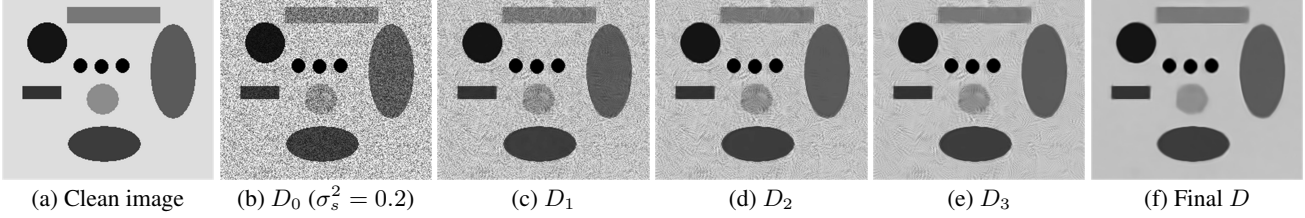
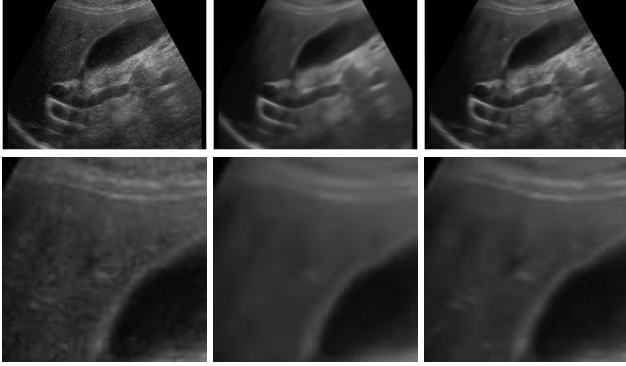


Figure 4: Our despeckled results in different iterations of the final recovery process.



(a) Input image (b) Original RPCA (c) Our model

Figure 5: Comparing RPCA [26] and our framework for low-rank recovery on a clinical ultrasound image.

Since large singular values usually correspond to major components of the matrix (important image features) while small singular values usually correspond to noise, a natural way is to set w_i to be inversely proportional to the magnitude of the singular value [9] and to zeroize the w_i 's corresponding to the smallest singular values; hence, we define

$$w_i = \begin{cases} 0 & \text{if } i \leq \lambda \\ \frac{\theta\sqrt{K+1}}{\sqrt{\sigma_i(\Psi_D)+\varepsilon}} & \text{otherwise} \end{cases}, \quad (6)$$

where λ and θ are parameters, and ε is set to be 0.00001 to avoid division by zero. In all the experiments, we empirically set λ as 9 and θ as $5\sqrt{2}$.

The initialization of $\sigma_i(\Psi_D)$. To iteratively solve Eq. 4 with TWNN, we need to initialize $\sigma_i(\Psi_D)$, but we do not have D at the beginning. Hence, before proceeding to iteratively minimize Eq. 4, we initialize $\sigma_i(\Psi_D)$ as

$$\sigma_i(\Psi_D) = \sqrt{\max(\sigma_i^2(\Psi_I) - \beta, 0)}, \quad (7)$$

where β is a parameter that estimates the noise component. We empirically set β as a value in [5, 50], using a larger β for ultrasound images with stronger noise.

Modeling the $\|\Psi_\eta\|_0$ term. Usually, this term is approximated by the L_1 norm, as in the RPCA method [26]. However, since the L_1 norm treats each element in Ψ_η independently, it does not take into account the spatial connections among groups of elements in Ψ_η . Hence, we propose

to employ the structured sparsity Ω_η [16, 13] to approximate $\|\Psi_\eta\|_0$ for ultrasound speckle reduction, since Ω_η can encode the structure prior knowledge of Ψ_η by involving overlapping submatrices in Ψ_η (which is actually a d^2 -by- $(K+1)$ matrix): $\Omega_\eta = \sum_{g \in \Psi_\eta} \|g\|_\infty$, where g is each 3×3 submatrix in Ψ_η ; and $\|\cdot\|_\infty$ is the maximum value over all the elements in g . Hence, each pair of adjacent groups (or submatrices) have six overlapping elements in Ψ_η .

Our model. By putting the TWNN (Eq. 5) and the structured sparsity (Ω_η) into Eq. 4, we obtained the final objective function to recover the underlying low-rank matrix:

$$\min_{\Psi_D, \Psi_\eta} \sum_{i=1}^M w_i \sigma_i(\Psi_D) + \alpha \sum_{g \in \Psi_\eta} \|g\|_\infty \text{ s.t. } \Psi_I = \Psi_D + \Psi_\eta, \quad (8)$$

where α is set to be 1.0 in the current implementation. In Fig. 5, we compare the despeckling performance of our method with the original RPCA [26]. Our method models the low-rank regularization term with the TWNN and the sparsity term using structure sparsity, so we can better preserve the features than that with the original RPCA.

Optimization. We have developed an efficient optimization procedure using the alternating direction method of multipliers (ADMM) to minimize the objective function in Eq. 8. Due to space limit, we provide the details of our optimization strategy in the supplemental material.

2.3. Final Recovery

The procedure outlined in Sec. 2.2 is applied iteratively. In the beginning of each subsequent iteration, we adopt an iterative regularization method [28, 9] to generate a new result by adding part of the filtered speckle noise back to the current despeckled image as follows:

$$I_h = D_{h-1} + \delta \cdot (I - D_{h-1}), \quad (9)$$

where I is the original ultrasound image; D_{h-1} is the despeckled result after $(h-1)$ iterations; and δ denotes the amount of filtered component that is to be added back to the result to avoid oversmoothing ($\delta=0.13$ in our experiments). The I_h is the generated ultrasound image with the iterative regularization in Eq. 9. Fig. 4 shows intermediate despeckled results of our method on a synthetic ultrasound image. As the iteration progresses, speckle noise is gradually suppressed while image features are revealed.

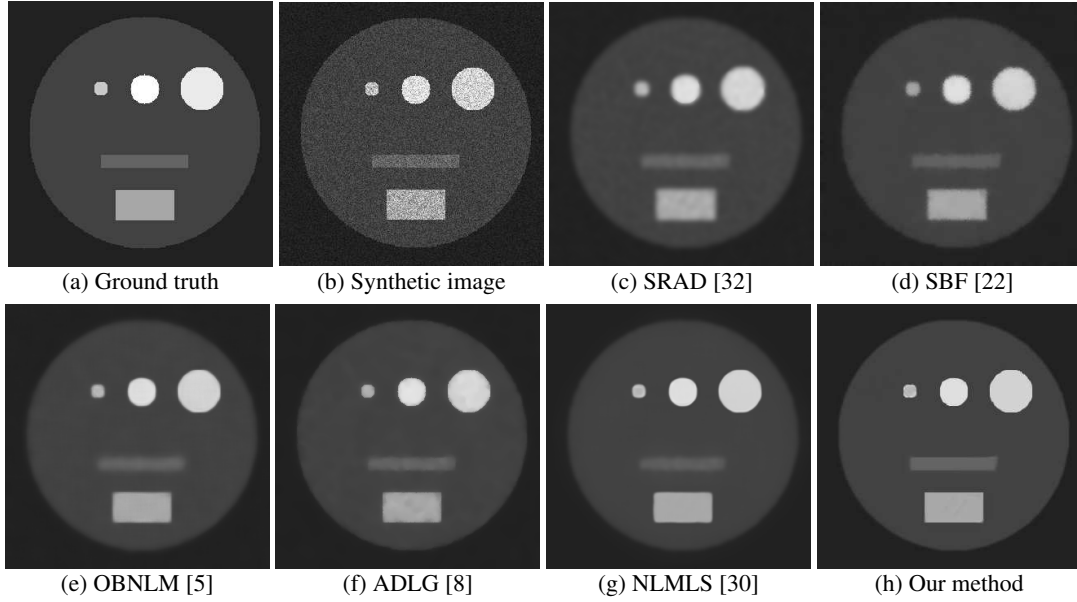


Figure 6: Comparing speckle reduction on an image with synthetic speckle noise. (a) Ground truth; (b) Synthetic image; Despeckled results by (c) SRAD [32] ($n=220$, $\Delta t=0.1$), (d) SBF [22] (25 iterations, patch size= 5×5), (e) OBNLM [5] ($h=2.9$, patch size= 9×9), (f) ADLG [8] ($n=90$, $\Delta t=0.1$), (g) NLMLS [30] ($h=0.8$, patch size= 9×9), and (h) our method ($\beta=15$, $H=15$).

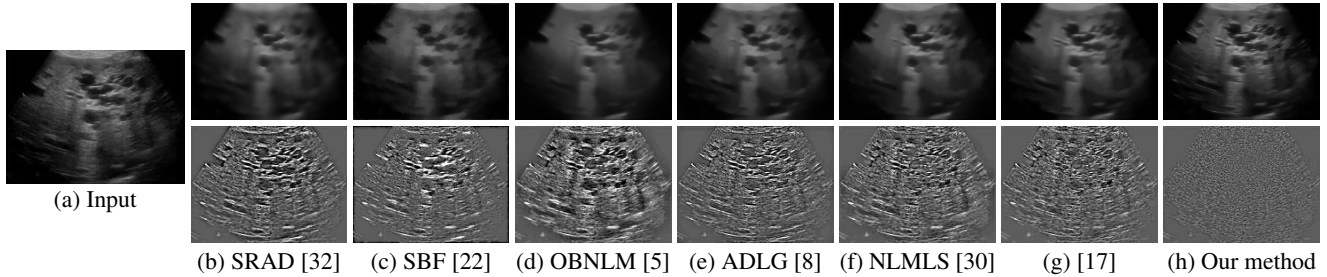


Figure 7: Comparison of speckle reduction on an ultrasound image with polycystic liver. (a) Original image; despeckled results and the removed speckle noise components by (b) SRAD [32] ($n=250$, $\Delta t=0.1$), (c) SBF [22] (10 iterations, patch size= 9×9), (d) OBNLM [5] ($h=1.5$, patch size= 9×9), (e) ADLG [8] ($n=200$, $\Delta t=0.25$), (f) NLMLS [30] ($h=0.4$, patch size= 9×9), (g) [17] ($mv=9$), and (h) our method ($\beta=10$, $H=10$). Each noise component image in the 2nd row is normalized to the same range for comparison. Our results show more features in the despeckled output and fewer features in our noise component than others.

3. Experiments

We evaluate the performance of our method on a number of synthetic and clinical ultrasound images by comparing with the following state-of-the-art despeckling filters: (1) speckle reducing anisotropic diffusion (SRAD) [32], (2) squeeze box filter (SBF) [22], (3) optimized Bayesian non-local means (OBNLM) [5], (4) anisotropic diffusion guided by Log-Gabor filters (ADLG) [8], and (5) non-local mean filter combined with local statistics (NLMLS) [30].

We evaluate our approach on a total of 60 clinical images: 20 liver images, 20 breast images, and 20 gall bladder images. See supplemental material for all the results. In our implementation, all but two parameters are fixed, so only β in Eq. 7 and the number of iterations (H) in the final recovery (see Sec. 2.3) need to be tuned. In detail, H is empirically set as [5, 10], depending on the noise lev-

el. The value of β also depends on the noise level, and we use a larger β for ultrasound images with high speckle noise level. For all the other methods, we also tune their associated parameters until we can produce the best result. We obtain code of SRAD, OBNLM, and ADLG from their project webpages. For SBF, we obtain its code from the author, while for NLMLS, we implement the method based on the paper. Noted that the source code of our method is publicly available at: https://sites.google.com/site/indexlzhou/webpage_despeckling_cvpr2017/index.

3.1. Synthetic Images

We first start with synthetic results, since it is possible to have quantitative measurements and comparisons.

Quantitative Metrics. We use five metrics to compare the performance of our method against others: peak signal-

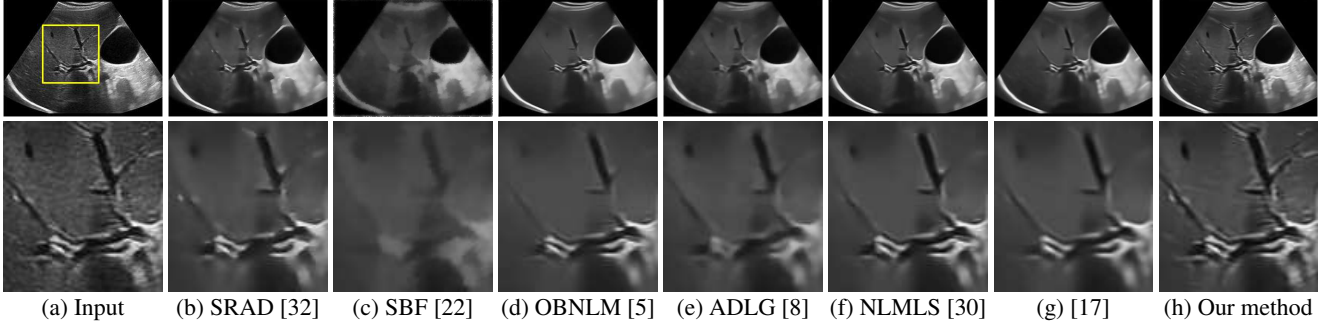


Figure 8: Comparing speckle reduction on an ultrasound image with a malignant papil tumor in bile duct. (a) Original image; results by (b) SRAD [32] ($n=130$, $\Delta t=0.1$), (c) SBF [22] (10 iterations, patch size= 5×5), (d) OBNNLM [5] ($h=1.2$, patch size= 9×9), (e) ADLG [8] ($n=110$, $\Delta t=0.15$), (f) NLMLS [30] ($h=0.3$, patch size= 9×9), (g) [17] ($mv=9$), and (h) our method ($\beta=10$, $H=10$).

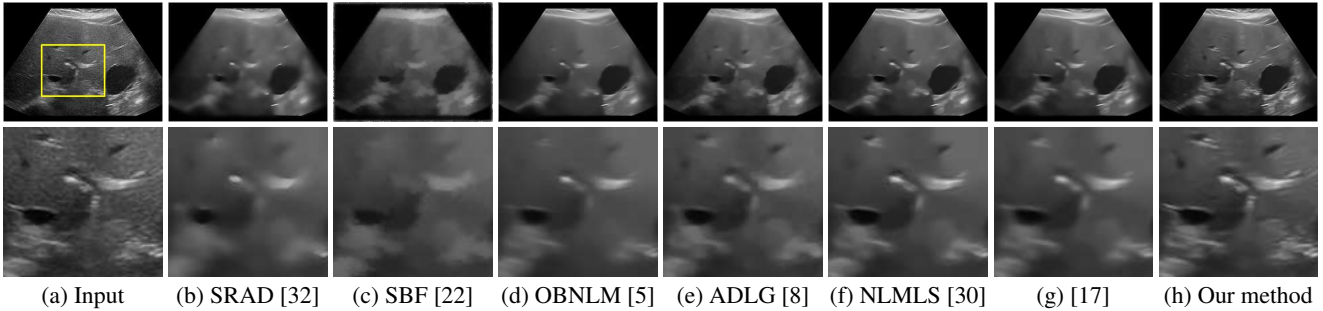


Figure 9: Comparing speckle reduction on an ultrasound image with multiple liver cysts at various sizes. (a) Original image; results by (b) SRAD [32] ($n=250$, $\Delta t=0.1$), (c) SBF [22] (15 iterations, patch size= 5×5), (d) OBNNLM [5] ($h=1.2$, patch size= 9×9), (e) ADLG [8] ($n=80$, $\Delta t=0.15$), (f) NLMLS [30] ($h=0.8$, patch size= 9×9), (g) [17] ($mv=9$), and (h) Our method ($\beta=10$, $H=10$).

Table 1: Quantitative comparison for results in Fig. 6.

	PSNR	FOM	UQI	SSIM	VIF
SRAD	27.72	0.4581	0.0965	0.9237	0.2730
SBF	28.35	0.5238	0.1970	0.9455	0.3618
OBNNLM	29.72	0.5207	0.1246	0.9484	0.3564
ADLG	30.02	0.7423	0.1318	0.9611	0.4138
NLMLS	30.32	0.7794	0.3951	0.9548	0.5403
Ours	32.75	0.9242	0.6933	0.9812	0.6964

Table 2: Comparison of PSNR values for despeckled results using synthetic noise on Fig. 6(a) at different noise levels.

	$\sigma_s^2 = 0.15$	$\sigma_s^2 = 0.2$	$\sigma_s^2 = 0.25$	$\sigma_s^2 = 0.3$
SRAD	26.64	25.56	25.08	23.75
SBF	27.75	26.04	25.65	23.89
OBNNLM	28.68	26.27	25.90	24.11
ADLG	28.97	27.08	26.56	24.59
NLMLS	29.14	27.98	27.13	26.48
Ours	30.77	29.60	28.42	27.61

to-noise ratio (PSNR), Pratt’s figure of merit (FOM) [32], universal quality index (UQI) [24], structural similarity (S-SIM) [25], and visual information fidelity (VIF) [21].

Results. For the purpose of quantitative comparisons, we generate noise over ground truth images by employing the synthetic speckle noise model in [5], which is a multiplicative Gaussian $\mathcal{N}(0, \sigma_s^2)$, where σ_s controls the noise level. We set σ_s^2 as 0.2, 0.2, and 0.1 for the cases shown in

Fig. 3 (bottom), Fig. 4, and Fig. 6, respectively. For the case of Fig. 6, we start with a clean image and add speckle noise to it; then we quantitatively compare the despeckled results of our method with SRAD, SBF, OBNNLM, ADLG, and NLMLS. Visual inspection shows our method better p-reserves boundaries compared to the other methods, while Table 1 reports the corresponding metric values for the despeckled results. Clearly, our method outperforms others for all the five metrics. High PSNR shows that our result is more consistent with the noise-free clean image. The high FOM shows that our method has better performance in terms of edge preservation. Our method also achieves the highest UQI, SSIM and VIF values, implying that our result has the best visual quality compared to others. Moreover, we test another four noise levels $\sigma_s^2 = \{0.15; 0.2; 0.25; 0.3\}$ on the same clean image over all the methods. Table 2 lists the resulting PSNR values, showing that our method achieves consistently high performance.

3.2. Clinical Images

We also visually compared our method with others on a number of clinical ultrasound images, including the despeckling methods [32, 22, 5, 8, 30], as well as the MRI Rician noise removal technique [17]. Noted that we use a similar framework as [17], but the way we construct the

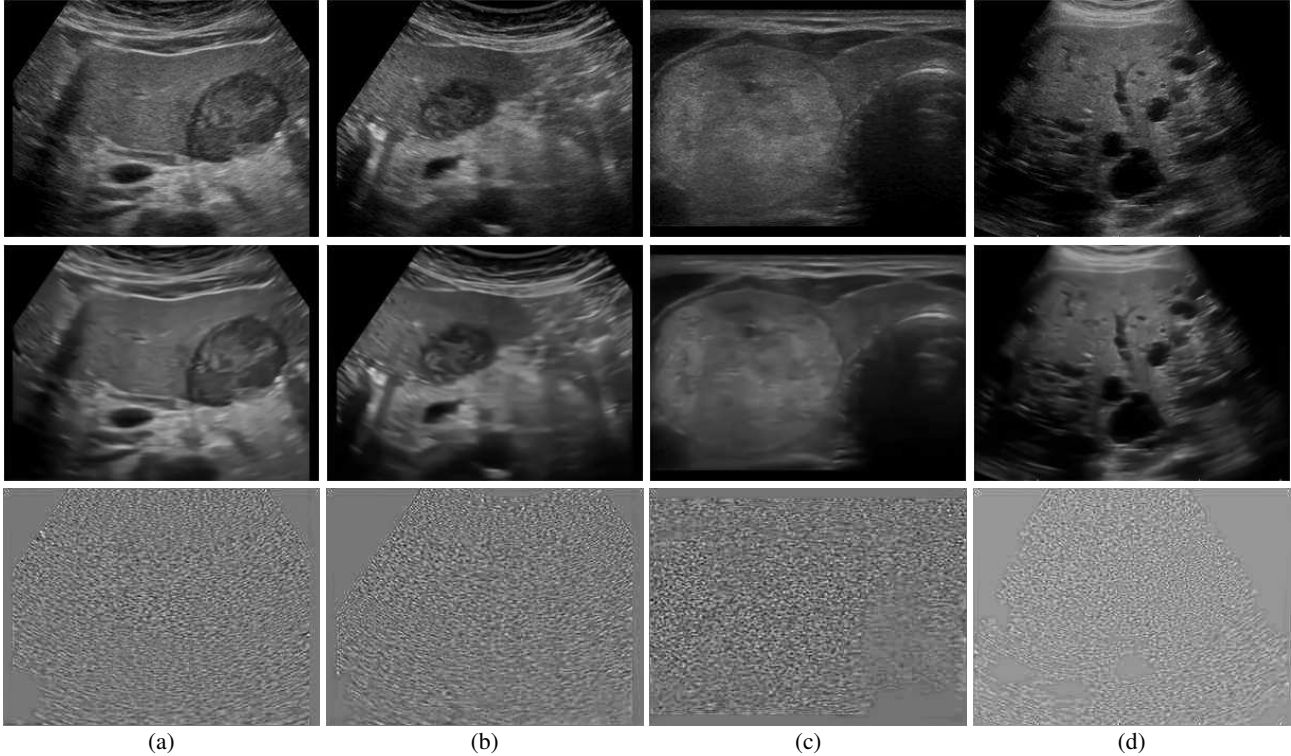


Figure 10: Despeckled results of our method on ultrasound images of four different tissue regions. First row: original images; second row: despeckled images; and third row: removed speckle noise component.

guidance image and the way we treat the low-rank noise are completely different. Fig. 7 shows a despeckling example on an ultrasound image with polycystic liver. We present the despeckled image and its removed speckle noise component in the first and second rows, respectively. Compared to others, including [17], our noise layer is more consistent and does not contain excessive structure details.

Two more comparisons on clinical images are shown in Fig. 8 and 9. After removing the speckle noise, our method produces better despeckling results by preserving image features, while others tend to oversmooth those features, see also the blown-up views in Fig. 8 and 9. Fig. 10 presents another four results on different tissues. Obviously, our method can consistently preserve features in different ultrasound images and effectively remove speckle noise. Noted that for clinical images there is no ground truth, so we cannot perform quantitative evaluation on the clinical images.

3.3. Pre-processing for Segmentation

Our method is also effective as a pre-processing step for the breast ultrasound (BUS) image segmentation. BUS is commonly used to distinguish between benign and malignant tumors that can be characterized by the shape or contour features of segmented breast lesions [19] [4] [8].

Quantitative Metrics. Four metrics are used to evaluate the segmentation accuracy: a combined accuracy of

Table 3: Mean values of segmentation metric AC, HD, HM and RMSD over results from ten breast ultrasound images.

	AC(%)	HD	HM	RMSD
Input	68.624	26.421	11.800	13.780
SRAD	89.719	17.844	3.310	5.266
SBF	90.649	17.311	3.080	5.008
OBNLM	91.283	14.595	2.743	4.340
ADLG	94.299	9.887	1.9354	2.9049
NLMLS	95.137	9.46	1.7467	2.704
Ours	97.563	4.159	1.142	1.425

Table 4: Same as Table 3, but using [18] instead of [15].

	AC(%)	HD	HM	RMSD
Input	88.38	17.748	3.937	5.809
SRAD	89.36	21.349	3.602	6.158
SBF	91.27	19.032	3.015	5.109
OBNLM	93.15	12.964	2.350	3.713
ADLG	94.08	11.403	2.057	3.232
NLMLS	94.29	10.755	2.089	3.152
Ours	96.46	3.929	1.305	1.548

true and false positive rate (AC) [3], Hausdorff distance (HD) [3], Hausdorff mean (HM) [3], and root mean square symmetric distance (RMSD) [11]. A good segmentation result should have large AC, and small HD, HM, and RMSD.

Experiments. We employ ten BUS images with different lesions, and six different methods (including ours) to despeckle them. Then, we segment the results (and inputs) by

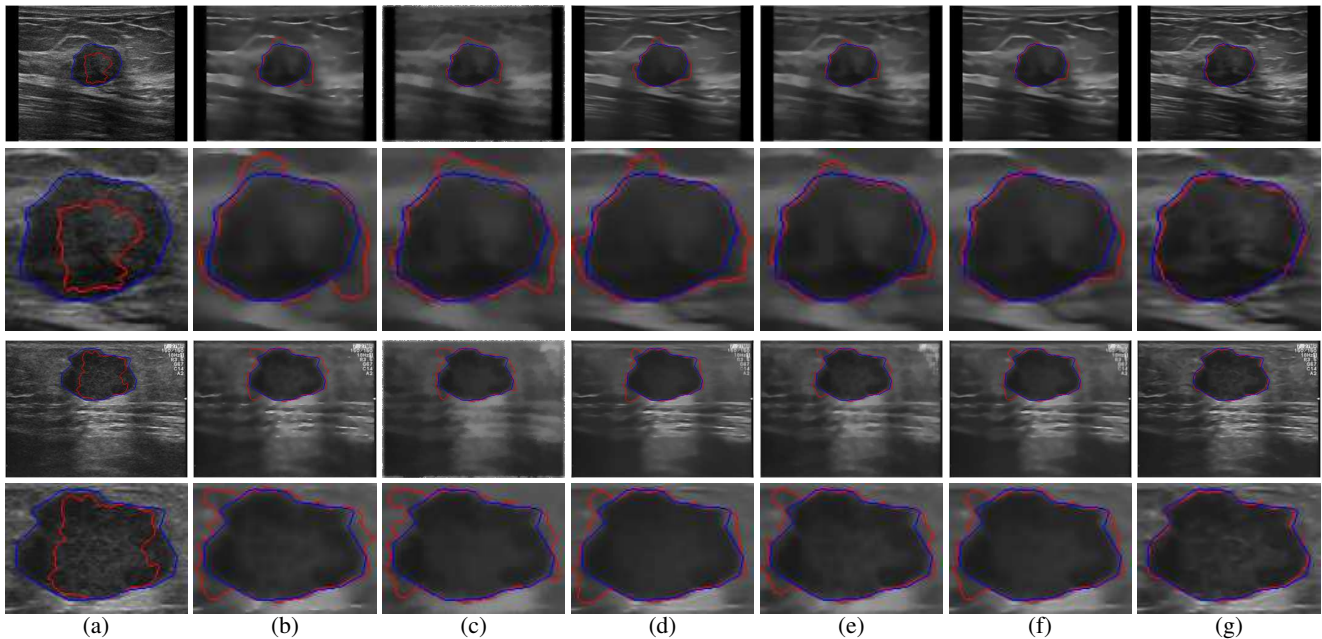


Figure 11: Comparing how various speckle reduction methods (b-g) help improve the accuracy of segmenting breast ultrasound images: an infiltrating ductal carcinoma (1st & 2nd rows) and metastases (3rd & 4th rows) . (a) Original image and its segmentation; despeckled results and the related segmentation results by (b) SRAD [32], (c) SBF [22], (d) OBNLM [5], (e) ADLG [8], (f) NLMLS [30], and (g) our method. Blue curves (all rows): the ground truth delineated by an experienced ultrasound physician. Red curves: segmentation results produced by [15] on input images and various despeckled results.

a level-set method by Li et al. [15] and a recent graph-cuts method by Peng et al. [18]. Fig. 11 shows two example BUS images (top two and bottom two rows), where the red curves are the segmentation results from Li et al. [15] (1st & 2nd rows), and the blue curves show the ground truth segmentations of the breast lesion boundaries; these segmentations were manually delineated by an experienced physician and are served as the ground truth for comparisons.

Results. From the results shown in Fig. 11, it is visually apparent that the original inputs are inferior due to the speckle noise’s interference, and our method gives the best performance as compared to other despeckling methods. In addition, we present results of the four quantitative metrics in Table 3 and 4 for segmentation using [15] and [18], respectively. One reason why the segmentation performances of the other methods degrade is that their results are more blur, and therefore, the level-set function is not able to more accurately stop at the lesion boundaries. For the case of graph cuts segmentation [18], it performs better on the raw input image as compared to the level-set method [15], but our method still outperforms other despeckling methods and gives the best segmentation result (see Table 4).

Acknowledgments. We thank reviewers for the valuable comments. Clinical images in paper and supplementary material are from a public data set: <http://www.ultrasoundcases.info>. This work was supported in part by the Research Grants Council of Hong Kong (Project No.

CUHK 14203115 and CUHK 14202514), the CUHK strategic recruitment fund and direct grant (4055061), the National Natural Science Foundation of China (Project No. 61233012), the Canada First Research Excellence Fund for the Vision: Science to Applications (VISTA) programme, and the Natural Science Foundation of Guangdong Province (Project No. 2014A030310381).

4. Conclusion

We propose a non-local low-rank filtering framework for speckle noise reduction. To overcome problems with non-local patch selection, we use a guidance image based on windowed inherent variation (WIV) filtering. To remove speckle noise within a group of similar patches, we decompose it into a low-rank component with a proposed truncated and weighted nuclear norm (TWNN) and a sparse component with the structured sparsity regularization. We also devise an efficient optimization based on the ADMM framework to solve the minimization. Both quantitative and qualitative evaluations on various synthetic and clinical images demonstrate that our method is able to effectively remove speckle noise and better preserve features compared with the state-of-the-art despeckling techniques. In addition, segmentation comparisons on a number of breast ultrasound images reveal that the despeckled results of our method can better facilitate breast lesion segmentation than results produced from the compared despeckling methods.

References

- [1] E. Amaldi and V. Kann. On the approximability of minimizing nonzero variables or unsatisfied relations in linear systems. *Theoretical Computer Science*, 209(1):237–260, 1998.
- [2] S. Balocco, C. Gatta, O. Pujol, J. Mauri, and P. Radeva. Srgb: Speckle reducing bilateral filtering. *Ultrasound in Medicine & Biology*, 36(8):1353–1363, 2010.
- [3] F. M. Cardoso, M. M. Matsumoto, and S. S. Furuie. Edge-preserving speckle texture removal by interference-based speckle filtering followed by anisotropic diffusion. *Ultrasound in Medicine & Biology*, 38(8):1414–1428, 2012.
- [4] H. Cheng, J. Shan, W. Ju, Y. Guo, and L. Zhang. Automated breast cancer detection and classification using ultrasound images: A survey. *Pattern recognition*, 43(1):299–317, 2010.
- [5] P. Coupé, P. Hellier, C. Kervrann, and C. Barillot. Nonlocal means-based speckle filtering for ultrasound images. *IEEE TIP*, 18(10):2221–2229, 2009.
- [6] W. Dong, G. Shi, Y. Ma, and X. Li. Image restoration via simultaneous sparse coding: Where structured sparsity meets gaussian scale mixture. *IJCV*, 114(2-3):217–232, 2015.
- [7] S. Esakkirajan, C. T. Vimalraj, R. Muhammed, and G. Subramanian. Adaptive wavelet packet-based de-speckling of ultrasound images with bilateral filter. *Ultrasound in Medicine & Biology*, 39(12):2463–2476, 2013.
- [8] W. G. Flores, W. C. de Albuquerque Pereira, and A. F. C. Infantosi. Breast ultrasound despeckling using anisotropic diffusion guided by texture descriptors. *Ultrasound in Medicine & Biology*, 40(11):2609–2621, 2014.
- [9] S. Gu, L. Zhang, W. Zuo, and X. Feng. Weighted nuclear norm minimization with application to image denoising. In *CVPR*, 2014.
- [10] Q. Guo, C. Zhang, Y. Zhang, and H. Liu. An efficient svd-based method for image denoising. *IEEE transactions on Circuits and Systems for Video Technology*, 26(5):868–880, 2016.
- [11] T. Heimann, B. Van Ginneken, M. Styner, Y. Arzhaeva, V. Aurich, C. Bauer, A. Beck, C. Becker, R. Beichel, G. Bekes, et al. Comparison and evaluation of methods for liver segmentation from ct datasets. *IEEE Transactions on Medical Imaging*, 28(8):1251–1265, 2009.
- [12] H. Ji, C. Liu, Z. Shen, and Y. Xu. Robust video denoising using low rank matrix completion. In *CVPR*, 2010.
- [13] K. Jia, T.-H. Chan, and Y. Ma. Robust and practical face recognition via structured sparsity. In *ECCV*, 2012.
- [14] K. Krissian, R. Kikinis, C.-F. Westin, and K. Vosburgh. Speckle-constrained filtering of ultrasound images. In *CVPR*, 2005.
- [15] C. Li, C. Xu, C. Gui, and M. D. Fox. Level set evolution without re-initialization: a new variational formulation. In *CVPR*, 2005.
- [16] J. Mairal, R. Jenatton, F. R. Bach, and G. R. Obozinski. Network flow algorithms for structured sparsity. In *NIPS*, 2010.
- [17] J. V. Manjón, P. Coupé, and A. Buades. MRI noise estimation and denoising using non-local PCA. *Medical image analysis*, 22(1):35–47, 2015.
- [18] B. Peng, L. Zhang, D. Zhang, and J. Yang. Image segmentation by iterated region merging with localized graph cuts. *Pattern Recognition*, 44(10):2527–2538, 2011.
- [19] G. Rahbar, A. C. Sie, G. C. Hansen, J. S. Prince, M. L. Melany, H. E. Reynolds, V. P. Jackson, J. W. Sayre, and L. W. Bassett. Benign versus malignant solid breast masses: Us differentiation 1. *Radiology*, 213(3):889–894, 1999.
- [20] G. Ramos-Llorden, G. Vegas-Sanchez-Ferrero, M. Martin-Fernandez, C. Alberola-Lopez, and S. Aja-Fernandez. Anisotropic diffusion filter with memory based on speckle statistics for ultrasound images. *IEEE TIP*, 24(1):345–358, 2015.
- [21] H. R. Sheikh and A. C. Bovik. Image information and visual quality. *IEEE TIP*, 15(2):430–444, 2006.
- [22] P. C. Tay, C. D. Garson, S. T. Acton, and J. A. Hossack. Ultrasound despeckling for contrast enhancement. *IEEE TIP*, 19(7):1847–1860, 2010.
- [23] B. Wang, T. Cao, Y. Dai, and D. C. Liu. Ultrasound speckle reduction via super resolution and nonlinear diffusion. In *ACCV*, 2009.
- [24] Z. Wang and A. C. Bovik. A universal image quality index. *Signal Processing Letters, IEEE*, 9(3):81–84, 2002.
- [25] Z. Wang, A. C. Bovik, H. R. Sheikh, and E. P. Simoncelli. Image quality assessment: from error visibility to structural similarity. *IEEE TIP*, 13(4):600–612, 2004.
- [26] J. Wright, A. Ganesh, S. Rao, Y. Peng, and Y. Ma. Robust principal component analysis: Exact recovery of corrupted low-rank matrices via convex optimization. In *NIPS*, 2009.
- [27] Q. Xie, Q. Zhao, D. Meng, Z. Xu, S. Gu, W. Zuo, and L. Zhang. Multispectral images denoising by intrinsic tensor sparsity regularization. In *CVPR*, 2016.
- [28] J. Xu and S. Osher. Iterative regularization and nonlinear inverse scale space applied to wavelet-based denoising. *IEEE TIP*, 16(2):534–544, 2007.
- [29] L. Xu, Q. Yan, Y. Xia, and J. Jia. Structure extraction from texture via relative total variation. *ACM TOG*, 31(6):139, 2012.
- [30] J. Yang, J. Fan, D. Ai, X. Wang, Y. Zheng, S. Tang, and Y. Wang. Local statistics and non-local mean filter for speckle noise reduction in medical ultrasound image. *Neurocomputing*, 195:88–95, 2016.
- [31] J. Yu, J. Tan, and Y. Wang. Ultrasound speckle reduction by a susan-controlled anisotropic diffusion method. *Pattern recognition*, 43(9):3083–3092, 2010.
- [32] Y. Yu and S. T. Acton. Speckle reducing anisotropic diffusion. *IEEE TIP*, 11(11):1260–1270, 2002.
- [33] Y. Zhan, M. Ding, L. Wu, and X. Zhang. Nonlocal means method using weight refining for despeckling of ultrasound images. *Signal Processing*, 103:201–213, 2014.
- [34] D. Zhang, Y. Hu, J. Ye, X. Li, and X. He. Matrix completion by truncated nuclear norm regularization. In *CVPR*, 2012.